

# Multiphysics analysis of RANS-based turbulent transport of solid fission products in the Molten Salt Fast Reactor

Andrea Di Ronco <sup>a</sup>, Stefano Lorenzi <sup>a</sup>, Francesca Giacobbo <sup>a</sup>, Antonio Cammi <sup>a,\*</sup>

<sup>a</sup> Department of Energy, Politecnico di Milano, Via La Masa 34, Milano 20156, Italy



## ARTICLE INFO

**Keywords:**  
 MSFR  
 Molten salt  
 Fission products  
 Multiphysics  
 Turbulence modeling  
 OpenFOAM

## ABSTRACT

The analysis of innovative reactor concepts such as the Molten Salt Fast Reactor (MSFR) requires the development of new modeling and simulation tools. In the case of the MSFR, the strong intrinsic coupling between thermal-hydraulics, neutronics and fuel chemistry has lead to the adoption of the multiphysics approach as a state-of-the-art paradigm. One of the peculiar aspects of liquid-fuel reactors such as the MSFR is the mobility of fission products (FPs) in the reactor circuit. Some FP species appear in form of solid precipitates carried by the fuel flow and can deposit on reactor boundaries (e.g., heat exchangers), potentially representing design issues related to the degradation of heat exchange performance or radioactive hotspots. Other precipitates might be present in the primary system as well, e.g. due to oxidation of fissile species which might lead to local criticality issues. The integration of transport models for solid particles in multiphysics codes is therefore relevant for the prediction of deposited fractions. To this aim, a previously developed Eulerian single-phase transport model is employed to analyze the distribution of solid FPs in two simplified MSFR-related geometries. The effect of physical parameters and of distributed particle sources on the numerical requirements needed to resolve particle concentration gradients at reactor boundaries in the considered geometries is investigated with the aid of analytical results. Analytical estimates of concentration gradients, even though not in full agreement with simulations, prove useful to drive the choice of adequate mesh refinements. Furthermore, the influence of different RANS turbulence modeling approaches on the prediction of particle distributions and deposition is tested. Results show a limited influence of the choice of turbulence models and parameters on the deposited fraction and on concentration gradients. As a result, it is found that deposition rates are scarcely affected by the choice of turbulent Schmidt number, with lower diffusivities being compensated by larger gradients. Large deposited fractions are indeed predicted, suggesting the efficiency of FPs transport mechanisms in the reactor and the need for the integration of adequate FPs transport models within state-of-the-art MSFR codes.

## 1. Introduction

The interest towards liquid-fuel reactor concepts has seen a significant increase over the last years. Among them, the fast-spectrum MSFR (Molten Salt Fast Reactor) (Serp et al., 2014), which was featured among the selected Generation IV reference technologies, has gained a leading role in the molten salt reactor research field thanks to its innovative design. The tight coupling among thermal-hydraulics, neutronics and fuel chemistry due to fuel circulation makes the MSFR system unique from the design and modeling viewpoints. The multiphysics approach has therefore become the standard tool for the development of computational models and to address the design and analysis of the MSFR (Tiberga et al., 2020). Multiphysics simulation codes have been

successfully employed to address several MSFR features, such as for instance the adoption of a bubbling system (Cervi et al., 2019), fuel compressibility effects (Cervi et al., 2019), the analysis of freeze-valve behavior (Tiberga et al., 2019). Multiphysics-based MSFR models have also been adopted to test the application of advanced data analysis and model order reduction techniques (German et al., 2020; Di Ronco et al., 2020).

Fission products (FPs) represent a major challenge in the modeling and design of the MSFR. They originate within the fuel and are not retained by solid structures, being thus free to be carried by the liquid fuel along the primary circuit. Some FP species are not expected to form stable compounds with the constituents of the fuel salt mixture (Grimes, 1970; Baes, 1974) and therefore may give rise to separate phases, either in the form of solid precipitates or gas bubbles. Solid FPs are likely to

\* Corresponding author.

E-mail address: [antonio.cammi@polimi.it](mailto:antonio.cammi@polimi.it) (A. Cammi).

<b>Nomenclature</b>	
<b>Latin symbols</b>	
$A_{r,g}^0$	reference g-th group, r-th neutron reaction cross-section log. coeff.
$C$	particle (vol.) concentration
$C_d$	deposited particle (surf.) concentration
$c_k$	k-th family del. neutron prec. (vol.) concentration
$c_p$	fluid specific heat capacity
$d_l$	l-th family decay heat prec. (vol.) concentration
$d_p$	particle diameter
$D$	laminar particle diffusivity
$D_{eff}$	effective particle diffusivity
$D_{n,g}$	g-th group neutron diffusion coefficient
$D_t$	turbulent particle diffusivity
$Da$	Damköhler number
$\bar{E}_{f,g}$	avg. g-th group fission energy
$g$	gravitational acceleration
$H$	channel half-width
$J_d$	particle (surf.) deposition flux
$k_B$	Boltzmann constant
$k_{eff}$	effective multiplication factor
$p$	fluid pressure
$Pr$	Prandtl number
$Pr_t$	turbulent Prandtl number
$q''$	vol. energy source
$S$	channel particle (vol.) source
$S_{max}$	channel max. particle (vol.) source
$S_{min}$	channel min. particle (vol.) source
$Sc$	Schmidt number
$Sc_t$	turbulent Schmidt number
$Sh$	Sherwood number
$T$	fluid temperature
$T_{sink}$	heat sink temperature
$T_0$	reference temperature (buoyancy)
$T_0^\Sigma$	reference temperature (group constants)
<b>u</b>	fluid velocity
$V_r$	heat removal region volume
$v_g$	avg. g-th group neutron velocity
$y$	channel transversal coord.
$\gamma_C$	fission yield of particles
<b>Greek symbols</b>	
$\alpha$	laminar thermal diffusivity
$\alpha_{eff}$	effective thermal diffusivity
$\alpha_t$	turbulent thermal diffusivity
$\beta_d$	total del. neutrons prec. fraction ( $\sum_k \beta_{d,k}$ )
$\beta_{d,k}$	k-th family del. neutron prec. fraction
$\beta_h$	total decay heat prec. fraction ( $\sum_l \beta_{h,l}$ )
$\beta_{h,l}$	l-th family decay heat prec. fraction
$\beta_T$	vol. thermal expansion coeff.
$\gamma$	deposition velocity
$\gamma_r$	heat removal coefficient
$\Delta y^*$	characteristic wall length
$\lambda_C$	particle decay constant
$\lambda_{d,k}$	k-th family del. neutron prec. decay constant
$\lambda_{h,l}$	l-th family decay heat prec. decay constant
$\nu$	laminar kinematic viscosity
$\nu_{eff}$	effective kinematic viscosity
$\nu_t$	turbulent kinematic viscosity
$\bar{\nu}_g$	avg. g-th group neutrons emitted per fission
$\rho$	fluid density
$\Sigma_{a,g}$	g-th group absorption cross-section
$\Sigma_{f,g}$	g-th group fission cross-section
$\Sigma_{r,g}$	g-th group, r-th neutron reaction cross-section
$\Sigma_{r,g}^0$	reference g-th group, r-th neutron reaction cross-section
$\Sigma_{s,g \rightarrow h}$	g-to-h-th group scattering cross-section
$\chi_{d,g}$	g-th energy group delayed neutron spectrum
$\chi_{p,g}$	g-th energy group prompt neutron spectrum
$\varphi_g$	g-th group integrated neutron flux

deposit on reactor surfaces in the form of solid precipitates (Kedl, 1972; Compere et al., 1975), giving rise to potential issues such as formation of localized decay heat sources as well as deterioration of heat exchanger performance. Surface deposits might also pose a serious radiological threat in inspection/maintenance operations. In a similar way, the oxidation of fissile species in particular operating conditions might lead to the formation of solid precipitates (Benes and Konings, 2012), with potential issues related to the transport and local accumulation of fissile particles. The analysis of FPs transport has found limited space in recent MSFR studies. In this regard, there has been focus on modeling the behavior and effects of Xenon transport in MSRs (Price et al., 2020; Carughi et al., 2022), while the analysis of metallic FPs in the context of a multiphysics system code for the study of the Molten Salt Reactor Experiment has been recently addressed by Walker and Ji (2021). The analysis of the MSFR by means of a traditional system-code approach is made difficult by its peculiar geometry and fuel circulation, making the use of high-fidelity models a more appropriate choice. A first approach for the integration of metallic FPs transport in a CFD-based multiphysics model has been described and verified against simplified analytical solutions in Di Ronco et al. (2021). Such approach is intended to allow for the analysis of inherently two-/three-dimensional effects, such as transport in complex turbulent flows, the estimation of particle deposition fluxes directly from concentration fields and the interaction with the gas bubbling system. Local temperature effects on precipitation of metallic species can also be directly taken into account, in view of

coupling with thermochemistry calculations (Marino et al., 2020).

The aim of this work is therefore the application of transport models for solid FPs integrated in state-of-the-art MSFR multiphysics tools to the preliminary analysis of FPs transport and deposition in relevant two-dimensional MSFR cases. Potential numerical issues arising from the commonly adopted “perfect adsorption” wall boundary conditions are addressed. Analytical results from Di Ronco et al. (2021) are used to illustrate such issues, and are compared to numerical simulation in a lid-driven cavity. Such case has been previously developed and studied in the context of benchmarking activities for multiphysics MSR codes (Tiberga et al., 2020). Then, due to their direct effect on species transport, different turbulence modeling approaches are tested in a more realistic MSFR case. The paper is organized as follows. The adopted multiphysics approach is briefly described in Section 2. The wall deposition problem is discussed, together with its analytical formulation, in Section 3. Section 4 describes the selected application cases, while Section 5 presents the results of the analysis together with some discussion. Conclusive remarks are finally reported in Section 6.

## 2. Multiphysics model

The OpenFOAM library (OpenFOAM, 2021), based on standard finite-volume methods for CFD calculations, is used to develop the numerical solver used in the present work. Originally developed for the transient analysis of the MSFR (Aufiero et al., 2014), the adopted

multiphysics solver was recently extended to allow for the study of compressibility effects during super-prompt-critical transients (Cervi et al., 2019) and of the bubbling system (Cervi et al., 2019; Caruggi et al., 2022). The version employed in this work features single-phase incompressible thermal-hydraulics, multi-group neutron diffusion and transport equations for delayed neutron and decay heat precursors. Transport equations for fission products are solved alongside the other physical modules, to provide a fully-coupled multiphysics simulation. All model equations are solved by means of finite-volume discretization, following an iterative segregated coupling approach.

### 2.1. Thermal-hydraulics model

Continuity, momentum and energy (in temperature form) conservation equations are expressed in a single-phase incompressible formulation:

$$\nabla \cdot \mathbf{u} = 0 \quad (1)$$

$$\frac{\partial \mathbf{u}}{\partial t} + \nabla \cdot (\mathbf{u} \mathbf{u}^T) = -\frac{1}{\rho} \nabla p + [1 - \beta_T(T - T_0)] \mathbf{g} + \nabla \cdot [\nu_{eff} (\nabla \mathbf{u} + (\nabla \mathbf{u})^T)] \quad (2)$$

$$\frac{\partial T}{\partial t} + \nabla \cdot (\mathbf{u} T) = \nabla \cdot (\alpha_{eff} \nabla T) + \frac{q'''}{\rho c_p} \quad (3)$$

where the quantities  $\mathbf{u}, p$  and  $T$ , which correspond to velocity, pressure and temperature, respectively, are intended as averaged in the sense of Reynolds-Averaged Navier-Stokes modeling. It follows that turbulence modeling is performed by means of standard linear eddy-viscosity based closure models, for which effective momentum and thermal diffusivities can be expressed as the sum of a laminar and a turbulent contribution:

$$\nu_{eff} = \nu + \nu_t \quad (4)$$

$$\alpha_{eff} = \alpha + \alpha_t = \frac{\nu}{Pr} + \frac{\nu_t}{Pr_t} \quad (5)$$

where  $Pr$  and  $Pr_t$  are the Prandtl and turbulent Prandtl numbers, respectively. Momentum and energy equations are coupled thanks to the Boussinesq approximation, for which the density value driving the buoyancy term in Eq. (2) is linearized around a reference temperature  $T_0$  and  $\beta_T$  represents the volumetric thermal expansion coefficient of the fluid. Except for what concerns density in the linearized buoyancy term, constant average values are used for thermophysical properties to keep the numerics and the coupling between different physics as simple as possible. Finally,  $q'''$  represents a volumetric energy source which includes internal heat generation (both prompt and delayed, see Eq. (10)) and optionally other energy sinks to model heat removal mechanisms.

### 2.2. Neutronics model

The multi-group diffusion model is adopted for neutron flux calculations (Hébert, 2010). Despite some limitations, it is widely employed in standard nuclear reactor analysis. Thanks to its relative simplicity and limited computational effort, it has found several successful applications especially for multiphysics analysis (Aufiero et al., 2014; Fiorina et al., 2016). More recent works have also proposed the extension of OpenFOAM-based multiphysics codes to more advanced neutron transport approaches, e.g. the SP3 model (Fiorina et al., 2017; Cervi et al., 2019). The diffusion equation for the  $g$ -th group-integrated neutron flux  $\varphi_g$  reads:

$$\frac{1}{v_g} \frac{\partial \varphi_g}{\partial t} = \nabla \cdot (D_{n,g} \nabla \varphi_g) - \Sigma_{a,g} \varphi_g - \sum_{h \neq g} \Sigma_{s,g \rightarrow h} \varphi_h + (1 - \beta_d) \chi_{p,g} \frac{\bar{\nu}_g}{k_{eff}} \Sigma_{f,g} \varphi_g + S_{n,g} \quad (6)$$

where  $S_{n,g}$  is the explicit neutron source of the  $g$ -th group, constituted by prompt fission and scattering neutrons from other groups and delayed neutron precursors decay:

$$S_{n,g} = (1 - \beta_d) \sum_{h \neq g} \chi_{p,h} \frac{\bar{\nu}_h}{k_{eff}} \Sigma_{f,h} \varphi_h + \sum_{h \neq g} \Sigma_{s,h \rightarrow g} \varphi_h + \chi_{d,h} \sum_k \lambda_{d,k} c_k \quad (7)$$

The presence of  $\varphi_h$  in the explicit source term  $S_{n,g}$  couples the transport equations for different energy groups, which are therefore dealt with following a segregated iterative approach. Most symbols have straightforward meaning and are listed in the Nomenclature section. It is worth mentioning that  $k_{eff}$  acts as a tunable multiplication factor to model a prescribed reactivity insertion. A power-iteration routine for the solution of the  $k$ -eigenvalue problem is also included for steady-state simulation, which allows for the iterative adjustment of  $k_{eff}$  to attain criticality at a specified power level.

Due to the circulating nature of the fuel, transport equations are formulated also for delayed neutron and decay heat precursors. The transport equation for the concentration of delayed neutron precursors of the  $k$ -th family  $c_k$  reads:

$$\frac{\partial c_k}{\partial t} + \nabla \cdot (\mathbf{u} c_k) = \nabla \cdot (D_{eff} \nabla c_k) - \lambda_{d,k} c_k + \beta_{d,k} \sum_g \bar{\nu}_g \Sigma_{f,g} \varphi_g \quad (8)$$

An analogous equation holds for the concentration of decay heat precursors of the  $l$ -th family  $d_l$ :

$$\frac{\partial d_l}{\partial t} + \nabla \cdot (\mathbf{u} d_l) = \nabla \cdot (D_{eff} \nabla d_l) - \lambda_{h,l} d_l + \beta_{h,l} \sum_g \bar{E}_{f,g} \Sigma_{f,g} \varphi_g \quad (9)$$

In the above equation, the actual concentration of decay heat precursors is multiplied by the average fission energy, such that  $d_l$  represents a volumetric amount of “latent” fission energy. Consistently, the volumetric heat source is given by:

$$q''' = (1 - \beta_h) \sum_g \bar{E}_{f,g} \Sigma_{f,g} \varphi_g + \sum_l \lambda_{h,l} d_l \quad (10)$$

For what concerns the diffusive transport of delayed neutrons and decay heat precursors, the diffusion coefficient  $D_{eff}$  is simply defined in analogy with momentum and thermal diffusivities as in Eq. (4 and 5):

$$D_{eff} = D + D_t = \frac{\nu}{Sc} + \frac{\nu_t}{Sc_t} \quad (11)$$

where  $Sc$  and  $Sc_t$  are the Schmidt and turbulent Schmidt numbers, respectively.

Group constants are adjusted as functions of local temperature around reference values to account for Doppler and fuel density effects. For a generic neutron reaction  $r$  occurring in the  $g$ -th energy group:

$$\Sigma_{r,g} = \left( \Sigma_{r,g}^0 + A_{r,g}^0 \log \frac{T}{T_0^\Sigma} \right) \frac{1 - \beta_T(T - T_0)}{1 - \beta_T(T_0^\Sigma - T_0)} \quad (12)$$

where Doppler effects are modeled by means of a logarithmic term where  $\Sigma_{r,g}^0$  and  $A_{r,g}^0$  respectively represent the cross-section and a corresponding logarithmic coefficient at a reference temperature  $T_0^\Sigma$ , whereas density effects are taken into account through a linear correction consistently with the buoyancy term. The reference temperature for cross-sections can be chosen independently from  $T_0$ . An analogous approach is employed for the correction of the intra-group neutron diffusion coefficient  $D_{n,g}$ . The quantities  $\Sigma_{r,g}^0$  and  $A_{r,g}^0$  are evaluated by means of the Monte Carlo reactor physics and burnup code SERPENT 2 (Leppänen et al., 2015).

### 2.3. Fission products transport model

Each fission product specie is modeled as a continuous scalar concentration field subject to advection, dispersion and decay mechanisms:

$$\frac{\partial C}{\partial t} + \nabla \cdot (\mathbf{u} C) = \nabla \cdot (D_{eff} \nabla C) - \lambda_C C + y_C \sum_g \Sigma_{f,g} \varphi_g \quad (13)$$

where  $C$  is the concentration of the species under consideration, expressed in number of particles per unit volume. Since we neglect chemical interactions and formation of separate phases, the source term is simply related to the fission rate through a suitable yield coefficient  $y_C$ .

The single-phase Eulerian approach is employed to limit the additional complexity of the computational model. It represents a valid approximation in many cases of interest, provided that particles are sufficiently small and do not interact among themselves (Guha, 2008). Previous experience with MSRs (Compere et al., 1975) suggests the validity of such modeling choice, at least at a first degree of approximation. The particle size can be used to derive a common expression for the laminar diffusivity  $D$ , which is given by the so-called Stokes–Einstein equation:

$$D = \frac{k_B T}{3\pi\rho\nu d_p} \quad (14)$$

where  $k_B$  is the Boltzmann constant and  $d_p$  is the particle diameter. The above equation is derived under the assumption of large Schmidt number  $Sc$  (Balboa Usabiaga et al., 2013) and can be used to estimate  $Sc$  in such limit:

$$Sc = \frac{3\pi\rho\nu^2 d_p}{k_B T} \quad (15)$$

It is worth mentioning that particle size plays a relevant role in determining particle diffusivity, according to the Stokes–Einstein relation. Particle sizes are determined by complex nucleation and growth mechanisms. Furthermore, size influences the relative role of inertial effects on momentum transport, invalidating the assumption of gradient-driven turbulent transport above certain diameter values. For the sake of simplicity, these modeling aspects are here neglected. In this work, we focus on the role of turbulence modeling on particle transport and we defer a sensitivity analysis on  $Sc$  to future developments.

As shown in (Di Ronco et al., 2021), particle–wall interaction mechanisms can be modeled separately from the bulk flow. This approach, which is valid under fairly general hypotheses on the nature of particle–wall interactions, assumes that relevant interactions only occur in a thin wall region whose influence can be collapsed in a first-order boundary conditions for the bulk flow (Prieve and Ruckenstein, 1976):

$$-D_{eff} \nabla C \cdot \mathbf{n} = \gamma C \quad (16)$$

for any point on the wall boundary, where  $\mathbf{n}$  denotes the outward pointing wall-normal direction. In this model, wall adsorption of FP particles is modeled through a single deposition parameter  $\gamma$ , which has the physical dimensions of a velocity.

### 3. Particle deposition with distributed sources

Before proceeding to the analysis of application cases, we discuss here some peculiar aspects of problems involving the transport of quantities subject to deposition boundary conditions and distributed internal generation. Distributed internal generation represents a modelling condition which is hardly found in common particle transport problems, and its effects on the concentration boundary layer need to be carefully addressed in CFD-based calculations. In particular, it is found that when deposition boundary conditions prescribe a vanishing species concentration at wall boundaries, large concentration gradients are to be expected if non-negligible generation of particles occurs in the boundary layer. This is naturally the case in MSFR calculations, where the fission rate does not vanish at reactor boundaries.

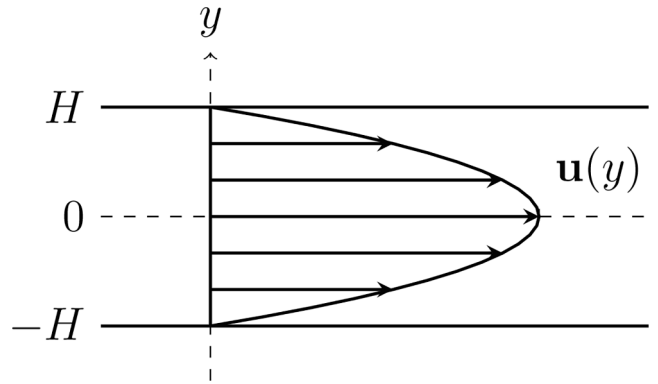


Fig. 1. Parallel plates channel geometry: with respect to the flow, the  $y$  coordinate denotes the transversal direction. Wall boundaries are located at  $y = \pm H$ .

To provide insight on this issue, analytical solutions for the scalar transport problem defined by Eq. (13) are found for simplified test cases. Albeit simplified, these results are useful to understand general features of expected solutions of more complex problems. The fully-developed parallel-plates transport problem Eq. (13) reduces to the 1D equation

$$D_{eff} \frac{d^2 C}{dy^2} - \lambda_C C + S(y) = 0 \quad (17)$$

equipped with the boundary conditions

$$\mp D_{eff} \frac{dC}{dy} = \gamma C, \quad y = \pm H \quad (18)$$

Here,  $y$  denotes the coordinate in the direction transversal to the channel-flow, and  $H$  is the half-width of the channel (Fig. 1).

The solution for a cosine-shaped source of the form

$$S(y) = S_{min} + (S_{max} - S_{min}) \cos\left(\frac{\pi}{2H}y\right) \quad (19)$$

reads

$$C(y) = \left(\frac{S_{max}}{\lambda_C}\right) K \left( e^{\frac{\sqrt{Da}}{H}y} + e^{-\frac{\sqrt{Da}}{H}y} \right) + \left(\frac{S_{max}}{\lambda_C}\right) \left[ \left(\frac{S_{min}}{S_{max}}\right) + \left(1 - \frac{S_{min}}{S_{max}}\right) \frac{4Da}{4Da + \pi^2} \cos\left(\frac{\pi}{2H}y\right) \right] \quad (20)$$

where

$$K = \frac{-\left(\frac{S_{min}}{S_{max}}\right) Sh + \left(1 - \frac{S_{min}}{S_{max}}\right) \left(\frac{\pi}{2}\right) \frac{4Da}{4Da + \pi^2}}{Sh(e^{\sqrt{Da}} + e^{-\sqrt{Da}}) + \sqrt{Da}(e^{\sqrt{Da}} - e^{-\sqrt{Da}})} \quad (21)$$

Non-dimensional quantities have been defined as  $Sh = \gamma H / D_{eff}$  and  $Da = \lambda_C H^2 / D_{eff}$ . Introducing some additional hypotheses, such as  $Sh \gg \sqrt{Da} \gg 1$ , it is possible to further simplify the solution:

$$C(y) = \left(\frac{S_{max}}{\lambda_C}\right) \left\{ \left(\frac{S_{min}}{S_{max}}\right) \left[ 1 - \frac{e^{\frac{\sqrt{Da}}{H}y} + e^{-\frac{\sqrt{Da}}{H}y}}{e^{\sqrt{Da}} + e^{-\sqrt{Da}}} \right] + \left(1 - \frac{S_{min}}{S_{max}}\right) \cos\left(\frac{\pi}{2H}y\right) \right\} \quad (22)$$

The role of the ratio  $S_{min}/S_{max}$  appears evident when considering the two extreme cases:

(A)  $S_{min}/S_{max} \rightarrow 0$ : the concentration profile tends to a simple cosine shape:

$$C(y) \rightarrow \left(\frac{S_{max}}{\lambda_C}\right) \cos\left(\frac{\pi}{2H}y\right) \quad (23)$$

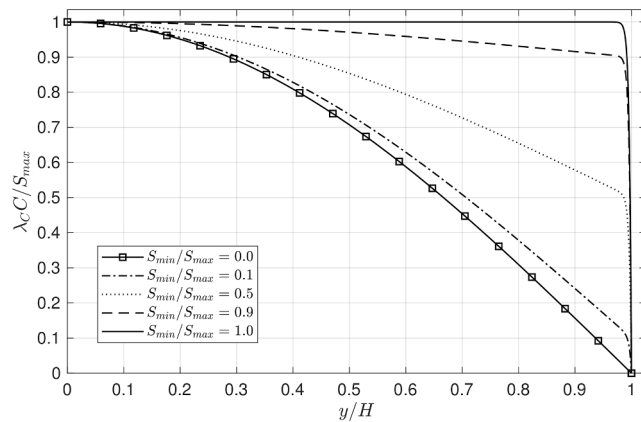


**Fig. 2.** Analytical solutions for the 1D parallel plates geometry. Different  $S_{min}/S_{max}$  ratios produce similar behaviors: the concentration profiles follow a cosine-shaped profile in the bulk flow, then drop to 0 in a thin region close to the wall boundary. The thickness  $\Delta y^*$  shows little dependence on  $S_{min}/S_{max}$ . For these cases,  $Da = 80000$ .

(B)  $S_{min}/S_{max} \rightarrow 1$ : the concentration profile tends to a uniform shape, except for a thin wall region where it quickly drops to 0:

$$C(y) \rightarrow \left( \frac{S_{max}}{\lambda_c} \right) \left( 1 - \frac{e^{\frac{\sqrt{Da}}{H}y} + e^{-\frac{\sqrt{Da}}{H}y}}{e^{\sqrt{Da}} + e^{-\sqrt{Da}}} \right) \quad (24)$$

Cases sufficiently far from (A) are significant for realistic reactor applications, where the “perfectly absorbing walls” condition ( $Sh \gg 1$ ) is assumed to adequately approximate particle-wall interactions and the distributed source does not vanish close to walls. It is easily demonstrated that, in such cases, the thickness of the wall layer where the concentration drop occurs is of the order of few times the characteristic length  $\Delta y^*$ , defined as

$$\Delta y^* = \frac{H}{\sqrt{Da}} = \sqrt{\frac{D_{eff}}{\lambda_c}} \quad (25)$$

For intermediate cases, the concentration profiles follow, in the bulk flow, a cosine shape whose extrapolated intersection at  $y = H$  depends on  $S_{min}/S_{max}$ , while they drop to 0 in the wall region much similarly to

the limiting case (B) (Fig. 2). The thickness  $\Delta y^*$  shows little dependence on  $S_{min}/S_{max}$  (except for cases very close to (A)), while mainly depends on physical parameters as described by Eq. (25).

For realistic physical parameters values, Eq. (25) predicts  $\Delta y^*$  values of the order of  $10^{-3}$  m or even less. Despite being strictly valid for simplified problems, these results offer a useful tool to understand the typical behavior of local concentration profiles close to walls also in more realistic cases. As anticipated, steep concentration gradients are therefore expected whenever homogeneous-Dirichlet-like boundary conditions are used in combination with distributed sources which do not vanish in the wall region. Particle deposition calculations in liquid-fuel reactors such as the MSFR fall under such conditions, and are therefore affected by relevant numerical consequences, as described in Section 4, since a grid size of the order of  $\Delta y^*$  or less is needed to correctly resolve the wall layer. We put emphasis on the role which wall gradients - and therefore the ability to resolve them - in determining the flux of deposited particles towards walls. From Eq. (16), the local deposition flux is defined as

$$J_d = -D_{eff} \nabla C \cdot \mathbf{n} \quad (26)$$

and, from a simple steady-state balance, the corresponding surface concentration of deposited particles reads

$$C_d = -\frac{D_{eff}}{\lambda_c} \nabla C \cdot \mathbf{n} \quad (27)$$

#### 4. Applications

The developed solver is tested on two different multiphysics cases. While in (Di Ronco et al., 2021) the implementation was verified against analytical results for a simplified channel geometry problem, here we seek the simulation of full multiphysics cases in more realistic MSFR-related geometries. In the first one, described in Section 4.1, we select a geometry based on the well-known lid-driven square laminar cavity. Even though still fairly simplified, the case features full coupling between thermal-hydraulics and neutronics. Geometry and parameters were chosen for an international benchmark for MSR codes (Tiberga et al., 2020), and this work may represent an extension of the MSFR benchmark towards solid FP simulation. In the second one, described in Section 4.2, a 2D MSFR geometry developed in the EVOL project is used. It features the loop structure typical of the MSFR with fuel recirculation, allowing for the simulation of more realistic turbulent cases. Both cases are selected for their simplified geometric features, which enable the

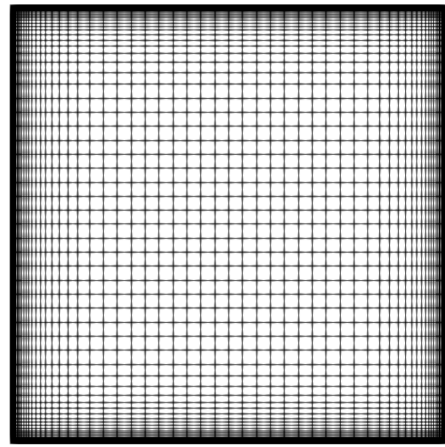
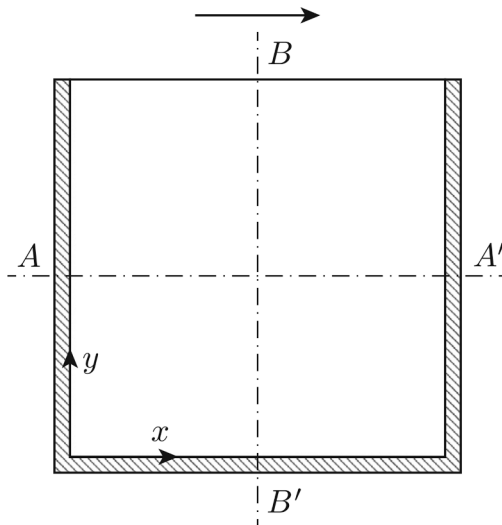


**Fig. 3.** Lid-driven cavity: geometry (from Tiberga et al. (2020), left) and computational mesh (coarsest case, right). The grid is refined by means of a constant growth-rate in the first 40 layers of cells, starting from a prescribed smallest layer size.

**Table 1**

Main physical parameter values adopted for the lid-driven cavity case (Tiberga et al., 2020).

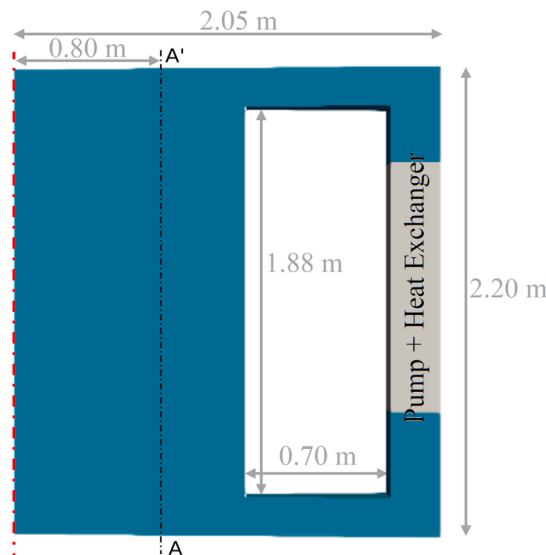
Parameter	Symbol	Units	Value
Density	$\rho$	$\text{kg m}^{-3}$	$2.0 \times 10^3$
Kinematic viscosity	$\nu$	$\text{m}^2 \text{s}^{-1}$	$2.5 \times 10^{-2}$
Specific heat capacity	$c_p$	$\text{J kg}^{-1} \text{K}^{-1}$	$3.075 \times 10^3$
Thermal expansion coeff.	$\beta_T$	$\text{K}^{-1}$	$2.0 \times 10^{-4}$
Ref. temperature	$T_0$	K	900
Prandtl number	$Pr$	—	$3.075 \times 10^5$
Schmidt number	$Sc$	—	$2.0 \times 10^8$
Heat removal coeff.	$\gamma_r$	$\text{W K}^{-1}$	$4.0 \times 10^6$
Heat sink temperature	$T_{sink}$	K	900

production of high-quality numerical grids even when wall refinement is crucial for the resolution of particle transport in the wall regions, as seen in Section 3. Furthermore, the adoption of 2D cases allows for a significant reduction of computational requirements with respect to full 3D simulations.

The physical properties needed for the simulation of FP particles are kept the same for each case to provide comparable results. The decay constant  $\lambda_C$  has been set to  $10^{-5} \text{ s}^{-1}$ , which corresponds to a nuclide half-life of approximately one day. The equivalent fission yield  $y_C$  has been set to  $10^{-2}$ . Such values are not specific to a particular nuclide, but have been chosen to mimic the behavior of the entire class of noble metal particles.

#### 4.1. Lid-driven cavity

The lid-driven cavity was recently employed to develop a reference case for a numerical benchmark of different multiphysics MSFR codes. A detailed description of the case and of the benchmark procedure can be found in (Tiberga et al., 2020). The domain is characterized by a 2 m by 2 m cavity filled with molten salt (Fig. 3). The domain is treated as a homogeneous, bare reactor. Therefore, standard vacuum conditions are applied for the neutron flux to each boundary, together with a (reflective) homogeneous Neumann condition for the delayed neutron precursors. Decay heat precursors are not simulated in this case, for better consistency with (Tiberga et al., 2020). The driving force for the liquid fuel flow is given by the upper lid, which moves at constant velocity of  $0.5 \text{ m s}^{-1}$ . All walls are treated as adiabatic, while energy is removed from the system through a simple volumetric heat sink:



$$q_r''' = -\frac{\gamma_r}{V_r}(T - T_{sink}) \quad (28)$$

where  $\gamma_r$  is a total heat removal coefficient and  $V_r$  is the volume of heat removal region, which in this case coincides with the entire cavity domain. The main physical case parameters are summarized in Table 1. Being the analysis conducted in steady-state conditions, simulations are performed in criticality eigenvalue mode with the integrated power normalized to 1000 MW.

With respect to the classic lid-driven case, the coupling with the distributed energy source through buoyancy significantly affects the flow pattern, producing more complex recirculation structures and making this test case suitable for study with multiphysics solvers, despite its overall simplicity.

The computational mesh is produced by specifying a small set of parameters: the number of divisions (equal in both directions), the thickness of the cells in the first boundary layer and the number of cells to be progressively refined. To correctly resolve the concentration boundary layers, a thickness of  $10^{-4} \text{ m}$  has been chosen according to results of the analytical analysis conducted in Section 3. The resolution of the boundary layer is particularly relevant for the correct prediction of the deposition rates. The prescribed refinement is found to adequately cover the boundary layer with several cell layers. The number of refined cells has been set to 40. For what concerns the number of divisions, three different values have been considered: 100, 200 and 400. Considering the two directions separately, the meshing routine computes a constant cell growth-rate which produces a smooth transition between the refined region and the rest of the domain (where the growth-rate is set to 1). Fig. 3 shows the mesh for the coarsest case (100 divisions).

#### 4.2. EVOL axisymmetric MSFR

A simplified 2D axisymmetric geometry is adopted following the work of the past EVOL project (Brovchenko et al., 2013). Solid parts in the system are neglected as well. The full geometry is shown in Fig. 4, together with some information regarding the position of the heat exchanger and pump sections. The heat exchanger is modeled similarly as in the cavity case, through the use of a linear sink term analogous to Eq. (28). The heat removal coefficient  $\gamma_r$  is here assumed to be zero outside the heat exchanger region. For what concerns the pump, a momentum source is imposed, along the vertical direction, which matches the flow rate at the pump outlet section to the total one ( $1.9 \times 10^4 \text{ kg}$

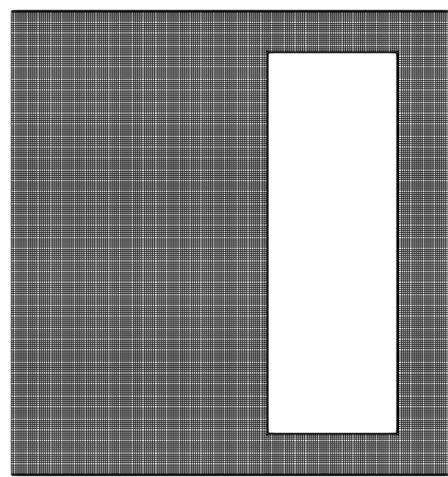


Fig. 4. EVOL case: an axisymmetric geometry (left) is chosen to reduce the computational requirements and the resulting mesh (right) is predominantly structured thanks to the simple geometry employed. Wall mesh refinement is obtained by subsequent divisions of the wall layer.

**Table 2**

Main physical parameter values adopted for the EVOL case.

Parameter	Symbol	Units	Value
Density	$\rho$	$\text{kg m}^{-3}$	$4.307 \times 10^3$
Kinematic viscosity	$\nu$	$\text{m}^2 \text{s}^{-1}$	$5.89 \times 10^{-6}$
Specific heat capacity	$c_p$	$\text{J kg}^{-1} \text{K}^{-1}$	$1.594 \times 10^3$
Thermal expansion coeff.	$\beta_T$	$\text{K}^{-1}$	$1.912 \times 10^{-4}$
Ref. temperature	$T_0$	K	973
Prandtl number	$Pr$	–	23.78
Turb. Prandtl number	$Pr_t$	–	0.85
Schmidt number	$Sc$	–	20.0
Turb. Schmidt number	$Sc_t$	–	0.50/0.85/1.20
Heat removal coeff.	$\gamma_r$	$\text{W m}^{-2} \text{K}^{-1}$	$2.5 \times 10^6$
Heat sink temperature	$T_{\text{sink}}$	K	900

$\text{s}^{-1}$ , for the entire reactor). The main physical case parameters are summarized in Table 2.

The simplified geometry allows for the production of good-quality structured meshes with little effort. In this case, a cell size of 0.01 m is employed across all the domain for the generation of the underlying mesh (Fig. 4). Then, subsequent cell divisions are applied to the first boundary layer of cells to provide a suitable mesh refinement in the wall region. Boundary layer cells are roughly halved 6 times, to produce a first layer with a thickness of approximately  $10^{-4}$  m. The total number of mesh elements is around  $4.2 \times 10^4$ .

Three different steady-state cases are simulated to assess the effect of turbulence modeling on the transport of FP particles. As described in Section 2.1, the solver makes use of the standard linear eddy viscosity approach for the modeling of turbulent quantities. The eddy viscosity  $\nu_t$  affects the transport problem in a direct way, through the definition of the total mass transfer coefficient  $D_{\text{eff}}$ , and through the computation of the velocity field. For this reason, three different turbulence models are used: standard  $k-\varepsilon$  (Launder and Spalding, 1974), the standard  $k-\omega$  (Wilcox, 2008) and the  $k-\omega$ -SST (Menter, 1994). Gradient-based turbulent diffusion constitutes a standard approach in CFD and multiphysics analysis, but relies heavily on the turbulent Schmidt number  $Sc_t$ , with optimal values depending on fluid properties and on flow configuration (Tominaga and Stathopoulos, 2007). Given the lack of experimental data for MSFR applications, in this work we select three different values (0.50, 0.85 and 1.20) to provide insight on the influence of such parameter on simulations over a relatively broad range of variation.

## 5. Results and discussion

### 5.1. Lid-driven cavity

Steady-state simulations have been performed with the three different mesh refinements described earlier. These preliminary laminar simulations have been conducted to study the effects of grid refinement. We stress that an adequate refinement is crucial for the prediction of deposition rates. For reference, velocity and temperature distributions are shown in Fig. 5. As anticipated, the interplay between the upper lid motion and the buoyancy effects produces complex recirculation patterns with two separate large laminar eddies, in contrast with the classical isothermal lid-driven cavity problem.

Concentration results for the different mesh refinements are reproduced in Fig. 6 and in Fig. 7 for what concerns distributions in the domain and profiles in the wall layers close to left and right walls, respectively. While the wall refinement guarantees a proper resolution of the wall layers in all cases, showing a suitable number of grid points even in the coarsest case thanks to the specific meshing procedure adopted which specifies the thickness of the first layer, only the most refined grid is able to capture all transport patterns in the domain. One possible cause is due to the use of gradient-limited upwind-biased 2nd-order divergence schemes. While 2nd-order schemes are needed to ensure proper accuracy, their use with low-quality meshes is known to produce poor results. On the other hand, the nature of the problem forces the use of upwind-biased schemes to provide a good balance between stability and accuracy, while gradient limiting is needed to ensure boundedness in the presence of steep gradients such as the ones which occur in the wall layers. Other transported quantities, such as neutron precursors, do not need this kind of numerical treatment due to the different reflective boundary conditions adopted.

Wall concentration profiles are characterized by different “asymptotic values” depending on the grid refinement and the overall accuracy dictated by the quality of the mesh. Nevertheless, within the wall layer, concentration profiles exhibit similar behavior, somewhat confirming some of the results given by the analytical treatment of Section 3. Using the values specified for  $\lambda_C$ ,  $\nu$  and  $Sc$ , Eq. (25) predicts a value for  $\Delta y^*$  of about 0.0035 m. Even though the mesh refinement has been selected to ensure fairly thinner boundary elements, such value is not found to be sufficiently representative of the results from Fig. 7. Computed profiles show significantly thinner wall layers, suggesting a strong influence of

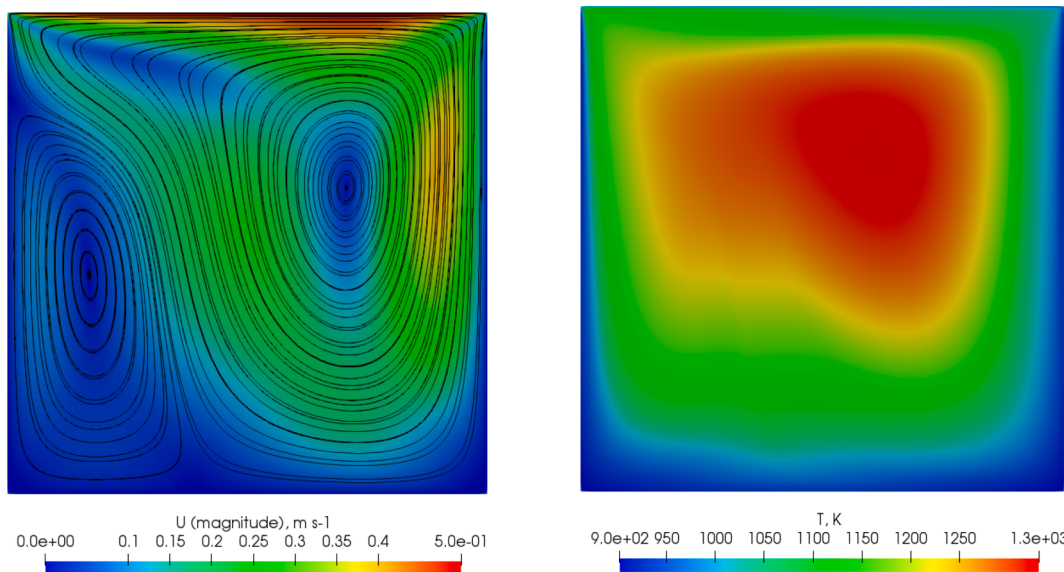
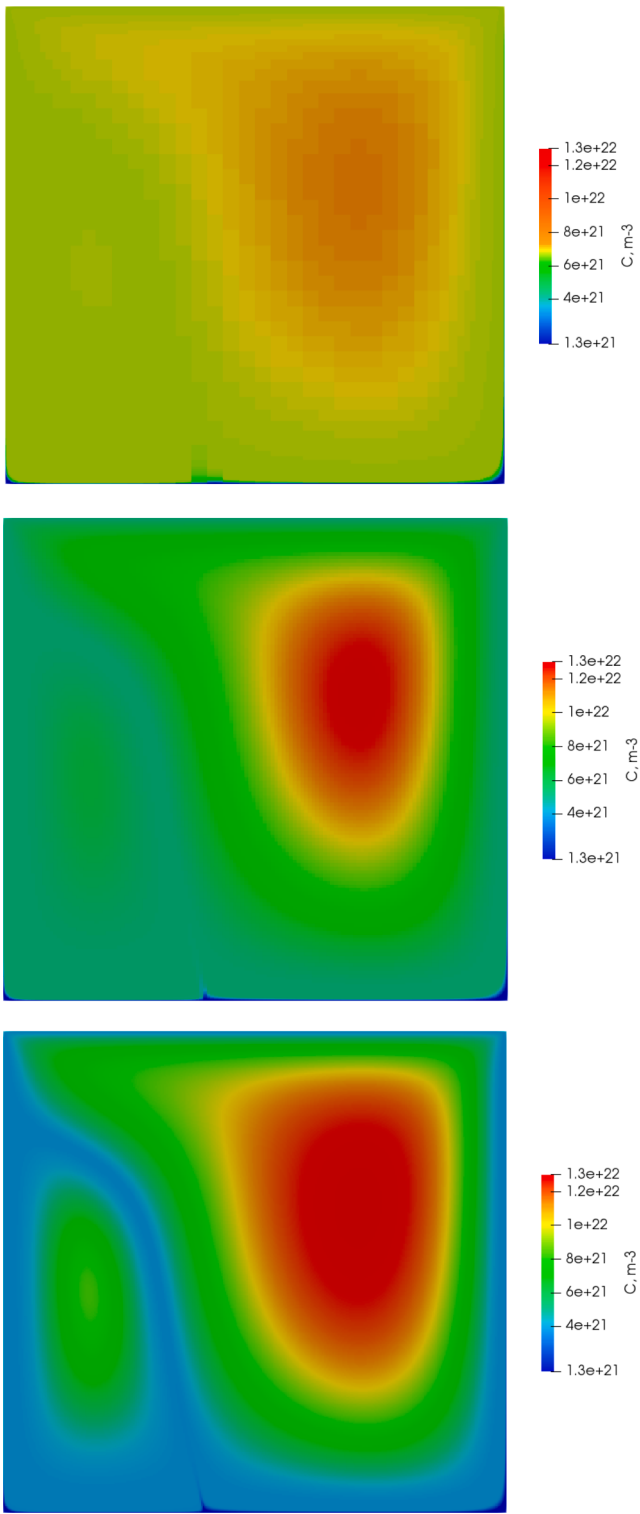
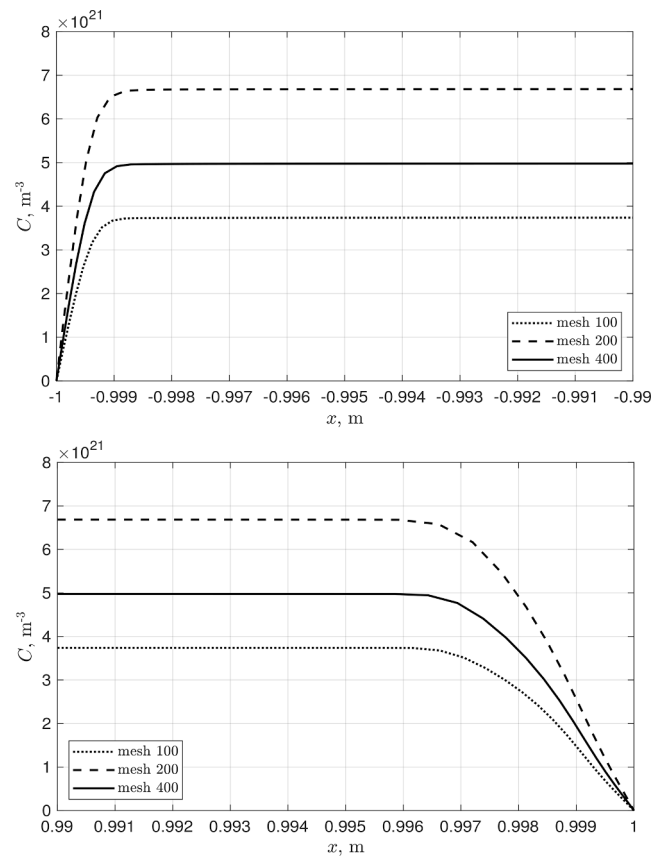


Fig. 5. Velocity  $U$  (left) and temperature  $T$  (right) distributions in the lid-driven cavity (most refined mesh, 400 divisions). Velocity streamlines are also added for more clarity. The combined action of lid motion and buoyancy affects the flow pattern, producing two separate recirculation zones.



**Fig. 6.** Particle concentration  $C$  distributions for three different mesh refinements: from top to bottom, 100, 200, and 400 divisions in both directions.

local velocity patterns and transport mechanism with respect to the simplified approach adopted in the analytical model. This is particularly evident from the comparison between the left and right walls, where the right wall layer is approximately 3–4 times larger than the left one. Nevertheless, the analytical treatment proves a useful tool to predict estimates and to understand the role of the main physical parameters.



**Fig. 7.** Particle concentration  $C$  wall profiles for three different mesh refinements. Line plots correspond to a horizontal line at half the cavity height on the left (top plot) and right (bottom plot) walls, corresponding to points A and A' of Fig. 3.

## 5.2. EVOL axisymmetric MSFR

Steady-state simulations have been conducted with the selected turbulence models and values for  $Sc_t$  for a total of nine cases, as described earlier. As in the cavity cases, 2nd-order upwind-biased gradient-limited convergence schemes have been used for the simulation of FPs. For reference, velocity and total kinetic viscosity distributions are shown in Fig. 8. As expected, the choice of turbulence model has an evident impact on the prediction of  $U$  and  $\nu_{eff}$ , in particular when comparing turbulence models from the  $k-\varepsilon$  and  $k-\omega$  families. Such differences have a direct influence on the combined effect of advective and diffusive transport mechanisms for FPs, as better evidenced by Fig. 9, which shows the volume distributions of the particle concentration  $C$  for the three simulated cases. Maximum and average particle concentrations are approximately one order of magnitude lower in the  $k-\varepsilon$  case than in the other cases, qualitatively in accordance with the higher  $k-\varepsilon$  diffusivity.

The same behavior is observed, naturally, in the concentration profiles close to walls. Fig. 10 shows concentration profiles close to the bottom and top walls, in correspondence of a vertical line placed at 0.8 m from the reactor symmetry axis (Fig. 4). Also in this case, gradient limiting allows for the computation of steep wall gradients without the insurgence of instability issues, while the prescribed mesh refinement proves adequate to resolve correctly the gradients. Once again, the thickness of the wall layers shows values of the order of  $10^{-3}$  m, which clearly demonstrates the importance of local velocity profiles and of turbulence in determining the steepness of the concentration gradients and thus the required grid refinement in the wall regions. It appears evident that also the choice of turbulence model itself affects to some

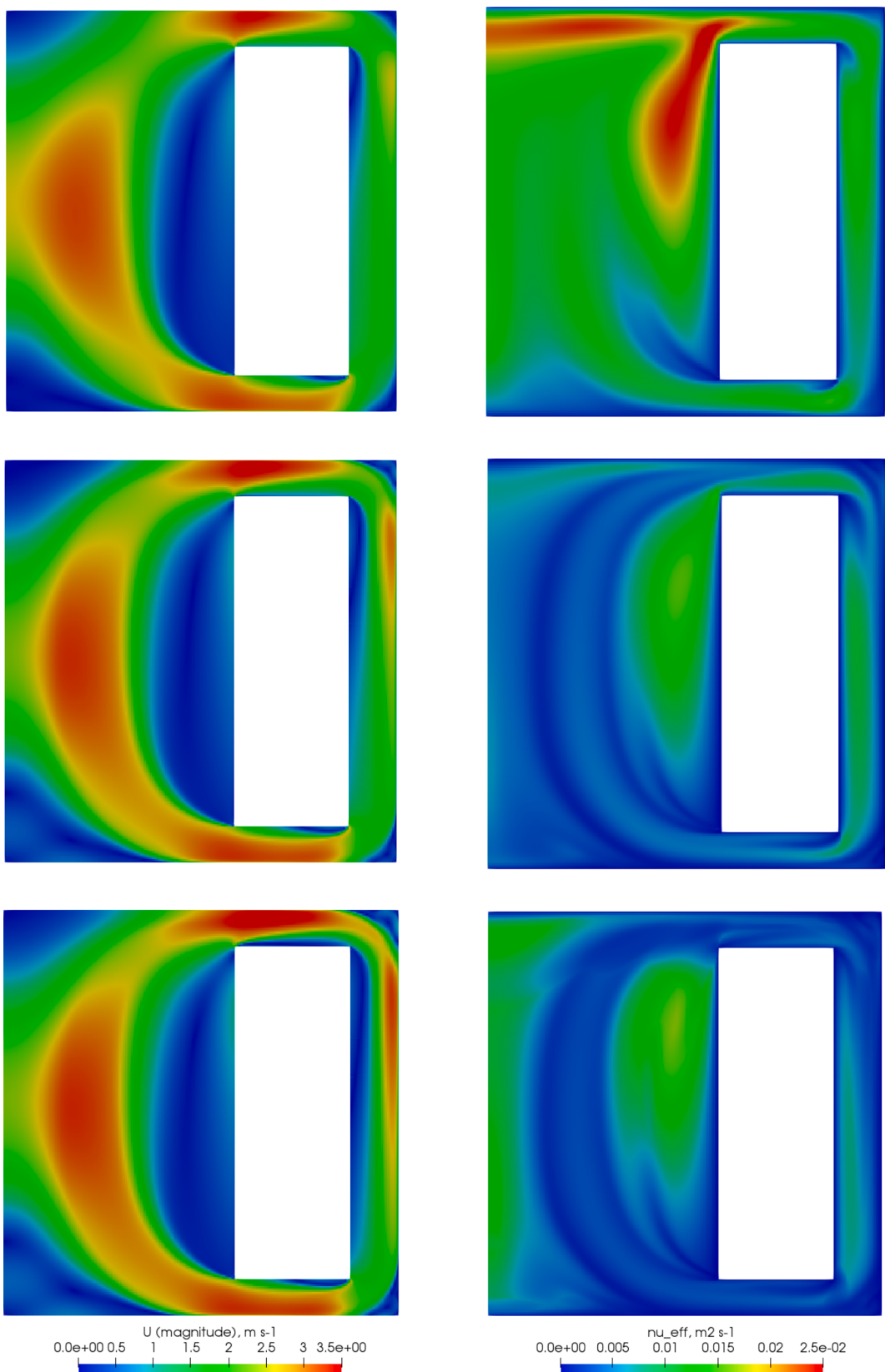


**Fig. 8.** Magnitude of velocity  $\mathbf{u}$  (left) and total kinetic viscosity  $\nu_{eff}$  (right) distributions in the EVOL reactor for the  $k-\varepsilon$ ,  $k-\omega$  and  $k-\omega-SST$  turbulence models (from top to bottom).

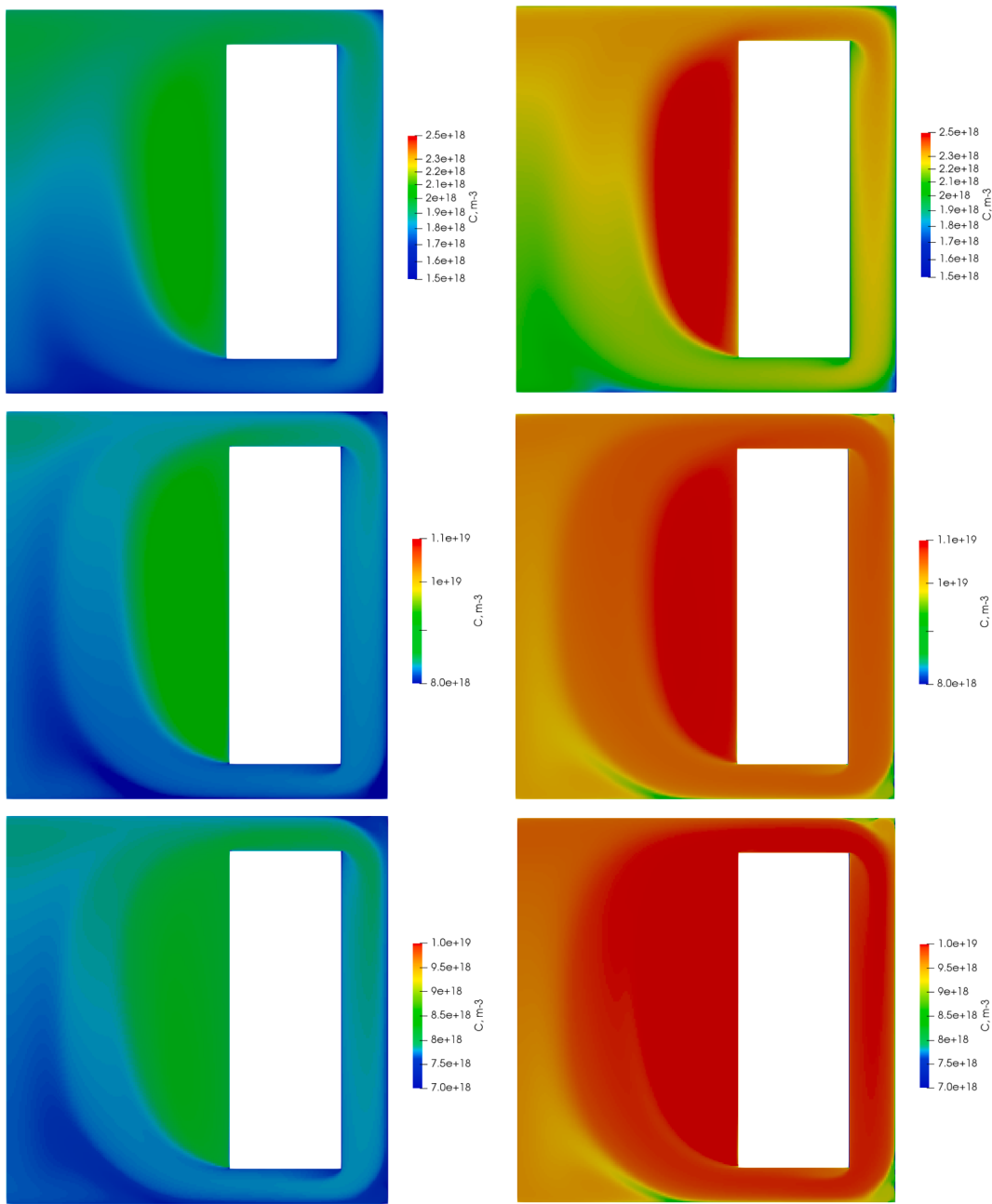


**Fig. 9.** Particle concentration  $C$  distributions for the  $k-\epsilon$ ,  $k-\omega$  and  $k-\omega$ -SST turbulence models (from top to bottom). Plots on the left and right columns refer to  $Sc_t$  equal to 0.50 and 1.20, respectively.

degree the thickness of the wall layers. Nevertheless, also in this case the thickness values predicted by the analytical model have proven useful, at least as preliminary estimates.

The integrated deposited fraction, together with other integral information are reported in Table 3. It appears from the results that, besides the differences in the total number of precipitate particles between the three cases, the choice of the turbulence model has a very limited influence on the number of deposited particles. This is a direct consequence of the similar gradients computed by the three models. Furthermore, in the diffusive wall layers the eddy diffusivity tends to zero and therefore the total value tends to the laminar one ( $\nu/Sc = 2.945 \cdot 10^{-7} \text{ m}^2 \text{ s}^{-1}$ ), which is the same for the three cases.

The choice of the turbulent Schmidt number appears to play a similar role: larger values lead to lower diffusivities and increased precipitate concentrations, but deposition rates are scarcely affected. This confirms

the prevalence of laminar diffusion in transport mechanisms close to walls, as shown by the similar wall concentration profiles shown in Fig. 10, and allows for a certain flexibility in the choice of  $Sc_t$  as far as deposition figures are concerned. Lastly, the transport mechanisms towards the walls appear efficient when compared to the intensity of radioactive decay (in our cases,  $\lambda_C = 10^{-5} \text{ s}^{-1}$ ), since more than 99.9% of particles end up depositing on walls. This effect is expected to be even more significant for longer-lived metallic FPs.

## 6. Conclusions

In this paper, previously developed transport models for the solid fission products in the MSFR have been tested on two separate molten salt cases, namely the lid-driven cavity problem and the EVOL geometry. The employed models are based on a Eulerian single-phase framework,

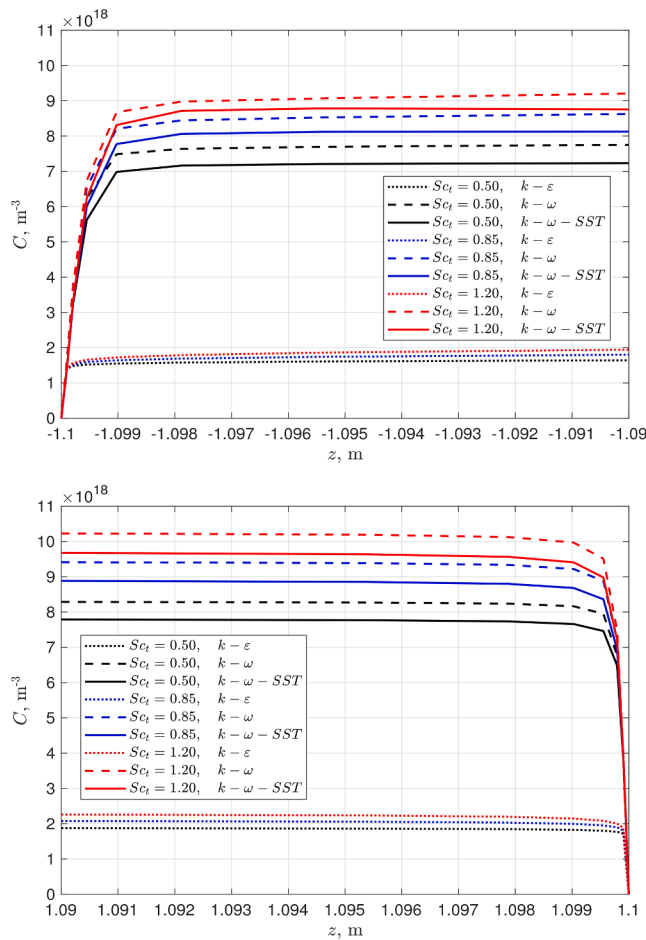


**Fig. 10.** Particle concentration  $C$  wall profiles for different values of the turbulent Schmidt number  $Sc_t$  and turbulence models. Line plots correspond to vertical lines of length 0.01 m placed at 0.8 m from the reactor symmetry axis on the bottom (top plot) and top (bottom plot) walls (see points A and A' of Fig. 4).

implemented in a consolidated MSFR multiphysics solver based on the open-source finite-volume library OpenFOAM. The main subjects of the investigation were the prediction of particle deposition fluxes and the analysis of related numerical issues arising from the commonly adopted assumption of “perfectly adsorbing” walls in combination with distributed particles source. The influence of different turbulence modeling approaches and turbulent diffusion parameters on particle distributions and deposition fluxes was also tested in the EVOL case.

Analytical results based on a simplified laminar parallel-plates geometry have been used to determine the expected particle concentration gradients close to solid walls. It was observed that the interplay between homogeneous Dirichlet boundary conditions and the presence of a non-negligible particle source in the wall layers produces steep gradients, and therefore poses the need for significant mesh refinement in the wall regions. Furthermore, the presence of steep gradients and the need to correctly resolve the boundary layers require, besides an adequate mesh refinement, the adoption of second order discretization schemes combined with gradient limiting to avoid numerical instability. Wall layer thicknesses in both the cavity and EVOL cases have not been found in complete agreement with the analytical estimate, demonstrating the role of geometry, local velocity profiles and of turbulence. However, prescribed mesh refinement based on the analytical model proved sufficient to adequately resolve wall concentration gradients in all simulated cases. The comparison of three different common turbulence models, namely the standard  $k-\epsilon$ , the standard  $k-\omega$  and the  $k-\omega-SST$

**Table 3**

EVOL case: main simulation results for the selected turbulence models and values of  $Sc_t$ . The balance error is computed as the relative difference between the integral source and the sum of the integral deposition and decay rates.

Quantity	Units	$k-\epsilon$	$k-\omega$	$k-\omega-SST$
$Sc_t = 0.50$				
Total precipitate	-	$4.8516678 \times 10^{17}$	$2.1769658 \times 10^{18}$	$2.0492698 \times 10^{18}$
Total deposit	-	$1.2627549 \times 10^{21}$	$1.2610617 \times 10^{21}$	$1.2611896 \times 10^{21}$
Total source	$s^{-1}$	$1.2632382 \times 10^{16}$	$1.2632367 \times 10^{16}$	$1.2632370 \times 10^{16}$
Total deposition rate	$s^{-1}$	$1.2627549 \times 10^{16}$	$1.2610617 \times 10^{16}$	$1.2611896 \times 10^{16}$
Total decay rate	$s^{-1}$	$4.8516678 \times 10^{12}$	$2.1769658 \times 10^{13}$	$2.0492698 \times 10^{13}$
Rel. balance error	-	$-1.5241115 \times 10^{-6}$	$-1.5441926 \times 10^{-6}$	$-1.5458692 \times 10^{-6}$
$Sc_t = 0.85$				
Total precipitate	-	$5.4409856 \times 10^{17}$	$2.4950726 \times 10^{18}$	$2.3620182 \times 10^{18}$
Total deposit	-	$1.2626960 \times 10^{21}$	$1.2607436 \times 10^{21}$	$1.2608769 \times 10^{21}$
Total source	$s^{-1}$	$1.2632381 \times 10^{16}$	$1.2632367 \times 10^{16}$	$1.2632370 \times 10^{16}$
Total deposition rate	$s^{-1}$	$1.2626960 \times 10^{16}$	$1.2607436 \times 10^{16}$	$1.2608769 \times 10^{16}$
Total decay rate	$s^{-1}$	$5.4409856 \times 10^{12}$	$2.4950726 \times 10^{13}$	$2.3620182 \times 10^{13}$
Rel. balance error	-	$1.5586352 \times 10^{-6}$	$1.5458756 \times 10^{-6}$	$1.5454547 \times 10^{-6}$
$Sc_t = 1.20$				
Total precipitate	-	$5.9885298 \times 10^{17}$	$2.7344317 \times 10^{18}$	$2.5986233 \times 10^{18}$
Total deposit	-	$1.2626413 \times 10^{21}$	$1.2605042 \times 10^{21}$	$1.2606403 \times 10^{21}$
Total source	$s^{-1}$	$1.2632382 \times 10^{16}$	$1.2632367 \times 10^{16}$	$1.2632370 \times 10^{16}$
Total deposition rate	$s^{-1}$	$1.2626413 \times 10^{16}$	$1.2605042 \times 10^{16}$	$1.2606403 \times 10^{16}$
Total decay rate	$s^{-1}$	$5.9885298 \times 10^{12}$	$2.7344317 \times 10^{13}$	$2.5986233 \times 10^{13}$
Rel. balance error	-	$-1.5255000 \times 10^{-6}$	$-1.5445096 \times 10^{-6}$	$-1.5561749 \times 10^{-6}$

models, with different turbulent Schmidt number values has shown a significant influence on the particle concentration distributions, given the discrepancies in the predicted velocity and eddy diffusivity fields. However, the deposition rates, which are one of the main subjects of the analysis, were much less affected, suggesting a certain flexibility in the choice of turbulence models and parameters as far as deposition is concerned. This effect is probably due to the fact that, in the concentration boundary layer, transport is dominated by diffusion and turbulent diffusivity tends to zero at walls. In connection with this aspect, it was found that, in steady-state conditions, a large fraction (more than 99.9%) of particles borne in the fuel are found on walls, demonstrating the efficiency of transport mechanisms within the reactor. This aspect might prove even more relevant when long-lived metallic species are considered, given the competition between the deposition and decay mechanisms in determining the fate of produced particles.

Despite relevant for the analysis of MSFR behavior, the adopted geometries were selected to simplify the numerical analysis and to reduce the computational requirements. Future work will include the analysis of FPs transport in a more realistic 3D reactor simulation. The study of the EVOL case has shown that the effect of turbulent transport in relatively complex geometries should not affect dramatically concentration gradients close to walls, giving reasonable estimates of the

required mesh refinement. Arbitrary and flexible mesh refinement in more complex 3D geometries, however, may prove a challenging task. Other possible extensions of the present work might include the adoption of more sophisticated turbulence modeling approaches such as Large Eddy Simulation. In this perspective, it is worth noting that preliminary work suggested that 3D models, especially following a LES approach, should require a significant increase in the cell count (above  $10^6$ ), with a computational cost in the range of several thousands CPU-hours for transients of a few tens of seconds. Regarding other limitations of the multiphysics transport model, the integration with a (possibly simplified) chemistry model to distinguish between the solid and the dissolved species might further improve the descriptive capabilities of the multiphysics tool. Finally, the effects of particles size on transport need to be addressed. Therefore, future developments should focus on such problem, possibly by considering the adoption of more sophisticated modeling approaches to take particle growth and inertial effects into account.

## Data availability statement

The data that support the findings of this study are openly available in Zenodo at [http://doi.org/10.5281/zenodo.5541560](https://doi.org/10.5281/zenodo.5541560).

## Funding

This project has received funding from the Euratom research and training programme 2014–2018 under grant agreement No. 847527.

## Disclaimer

The content of this paper does not reflect the official opinion of the European Union. Responsibility for the information and/or views expressed therein lies entirely with the authors.

## Declaration of Competing Interest

The authors declare that they have no known competing financial interests or personal relationships that could have appeared to influence the work reported in this paper.

## References

- Aufiero, M., Cammi, A., Geoffroy, O., Losa, M., Luzzi, L., Ricotti, M.E., Rouch, H., 2014. Development of an OpenFOAM model for the Molten Salt Fast Reactor transient analysis. *Chem. Eng. Sci.* 111, 390–401. <https://doi.org/10.1016/j.ces.2014.03.003>.
- Baes, C., 1974. The chemistry and thermodynamics of molten salt reactor fuels. *J. Nucl. Mater.* 51, 149–162. [https://doi.org/10.1016/0022-3115\(74\)90124-X](https://doi.org/10.1016/0022-3115(74)90124-X).
- Balboa Usabiaga, F., Xie, X., Delgado-Buscalioni, R., Donev, A., 2013. The Stokes-Einstein relation at moderate Schmidt number. *J. Chem. Phys.* 139, 214113 <https://doi.org/10.1063/1.4834696>.
- Beneš, O., Konings, R., 2012. Molten Salt Reactor Fuel and Coolant, in: Konings, R.J. (Ed.), *Comprehensive Nuclear Materials*. Elsevier, Oxford, pp. 359–389. doi: 10.1016/B978-0-08-056033-5.00062-8.
- Brovchenko, M., Merle Lucotte, E., Rouch, H., Alcaro, F., Allibert, M., Aufiero, M., Cammi, A., Dulla, S., Feynberg, O., Frima, L., Geoffroy, O., Ghetta, V., Heuer, D., Ignatiev, V., Kloosterman, J.L., Lathouwers, D., Laureau, A., Luzzi, L., Merk, B., Ravetto, P., Rineiski, A., Rubiolo, P., Rui, L., Szieberth, M., Wang, S., Yamaji, B., 2013. Optimization of the pre-conceptual design of the MSFR. Deliverable 2, 1–69.
- Carughi, F., Cammi, A., Cervi, E., Di Ronco, A., Lorenzi, S., 2022. Modelling and simulation of the gaseous fission product removal in the Molten Salt Fast Reactor, in: Proc. of the 19th Int. Topical Meet. on Nuclear Reactor Thermal Hydraulics (NURETH-19), American Nuclear Society, p. 35765.
- Cervi, E., Lorenzi, S., Cammi, A., Luzzi, L., 2019. Development of a multiphysics model for the study of fuel compressibility effects in the Molten Salt Fast Reactor. *Chem. Eng. Sci.* 193, 379–393. <https://doi.org/10.1016/j.ces.2018.09.025>.
- Cervi, E., Lorenzi, S., Cammi, A., Luzzi, L., 2019. Development of an SP3 neutron transport solver for the analysis of the Molten Salt Fast Reactor. *Nucl. Eng. Des.* 346, 209–219. <https://doi.org/10.1016/j.nucengdes.2019.03.001>.
- Cervi, E., Lorenzi, S., Luzzi, L., Cammi, A., 2019. Multiphysics analysis of the MSFR helium bubbling system: A comparison between neutron diffusion, SP3 neutron transport and Monte Carlo approaches. *Ann. Nucl. Energy* 132, 227–235. <https://doi.org/10.1016/j.anucene.2019.04.029>.
- Compere, E., Kirslis, S., Bohlmann, E., Blankenship, F., Grimes, W., 1975. Fission product behavior in the molten salt reactor experiment. Technical Report ORNL-4865, 4077644. Oak Ridge National Laboratory. doi: 10.2172/4077644.
- Di Ronco, A., Introini, C., Cervi, E., Lorenzi, S., Jeong, Y.S., Seo, S.B., Bang, I.C., Giacobbo, F., Cammi, A., 2020. Dynamic mode decomposition for the stability analysis of the Molten Salt Fast Reactor core. *Nucl. Eng. Des.* 362, 110529 <https://doi.org/10.1016/j.nucengdes.2020.110529>.
- Di Ronco, A., Lorenzi, S., Giacobbo, F., Cammi, A., 2021. An Eulerian Single-Phase Transport Model for Solid Fission Products in the Molten Salt Fast Reactor: Development of an Analytical Solution for Verification Purposes. *Front. Energy Res.* 9, 311. <https://doi.org/10.3389/fenrg.2021.692627>.
- Fiorina, C., Hursin, M., Pautz, A., 2017. Extension of the GeN-Foam neutronic solver to SP3 analysis and application to the CROCUS experimental reactor. *Ann. Nucl. Energy* 101, 419–428. <https://doi.org/10.1016/j.anucene.2016.11.042>.
- Fiorina, C., Kerkar, N., Mikityuk, K., Rubiolo, P., Pautz, A., 2016. Development and verification of the neutron diffusion solver for the GeN-Foam multi-physics platform. *Ann. Nucl. Energy* 96, 212–222. [https://doi.org/10.1016/j.anocene.2016.05.023](https://doi.org/10.1016/j.anucene.2016.05.023).
- German, P., Tano, M., Ragusa, J.C., Fiorina, C., 2020. Comparison of reduced-basis techniques for the model order reduction of parametric incompressible fluid flows. *Prog. Nucl. Energy* 130, 103551. <https://doi.org/10.1016/j.pnucene.2020.103551>.
- Grimes, W.R., 1970. Molten-salt reactor chemistry. *Nuclear Appl. Technol.* 8, 137–155. <https://doi.org/10.13182/NT70-A28621>.
- Guha, A., 2008. Transport and Deposition of Particles in Turbulent and Laminar Flow. *Annu. Rev. Fluid Mech.* 40, 311–341. <https://doi.org/10.1146/annurev.fluid.40.111406.102220>.
- Hébert, A., 2010. Multigroup neutron transport and diffusion computations, in: Cacuci, D.G. (Ed.), *Handbook of Nuclear Engineering*. Springer, US, Boston, MA, pp. 751–911. doi: 10.1007/978-0-387-98149-9\_8.
- Kedl, R.J., 1972. Migration of a class of fission products (Noble metals) in the molten-salt reactor experiment. Technical Report ORNL-TM-3884, 4471292. Oak Ridge National Laboratory. doi: 10.2172/4471292.
- Launder, B., Spalding, D., 1974. The numerical computation of turbulent flows. *Comput. Methods Appl. Mech. Eng.* 3, 269–289. [https://doi.org/10.1016/0045-7825\(74\)90029-2](https://doi.org/10.1016/0045-7825(74)90029-2).
- Leppänen, J., Pusa, M., Viitanen, T., Valtavirta, V., Kaltainenaho, T., 2015. The Serpent Monte Carlo code: Status, development and applications in 2013. *Ann. Nucl. Energy* 82, 142–150. <https://doi.org/10.1016/j.anucene.2014.08.024>.
- Marino, A., Peltomäki, M., Lim, J., Aerts, A., 2020. A multi-physics computational tool based on CFD and GEM chemical equilibrium solver for modeling coolant chemistry in nuclear reactors. *Prog. Nucl. Energy* 120, 103190. <https://doi.org/10.1016/j.pnucene.2019.103190>.
- Menter, F.R., 1994. Two-equation eddy-viscosity turbulence models for engineering applications. *AIAA J.* 32, 1598–1605. <https://doi.org/10.2514/3.12149>.
- OpenFOAM, 2021. The OpenFOAM Foundation. URL: <https://openfoam.org/>. [Online; accessed 5-August-2021].
- Price, T., Chvala, O., Bereznai, G., 2020. A dynamic model of xenon behavior in the Molten Salt Reactor Experiment. *Ann. Nucl. Energy* 144, 107535. [https://doi.org/10.1016/j.anocene.2020.107535](https://doi.org/10.1016/j.anucene.2020.107535).
- Prieve, D.C., Ruckenstein, E., 1976. Rates of deposition of brownian particles calculated by lumping interaction forces into a boundary condition. *J. Colloid Interface Sci.* 57, 547–550. [https://doi.org/10.1016/0021-9797\(76\)90232-0](https://doi.org/10.1016/0021-9797(76)90232-0).
- Serp, J., Allibert, M., Beneš, O., Delpech, S., Feynberg, O., Ghetta, V., Heuer, D., Holcomb, D., Ignatiev, V., Kloosterman, J.L., Luzzi, L., Merle-Lucotte, E., Uhlíř, J., Yoshioka, R., Zhimin, D., 2014. The molten salt reactor (MSR) in generation IV: Overview and perspectives. *Prog. Nucl. Energy* 77, 308–319. <https://doi.org/10.1016/j.pnucene.2014.02.014>.
- Tiberga, M., de Oliveira, R.G.G., Cervi, E., Blanco, J.A., Lorenzi, S., Aufiero, M., Lathouwers, D., Rubiolo, P., 2020. Results from a multi-physics numerical benchmark for codes dedicated to molten salt fast reactors. *Ann. Nucl. Energy* 142, 107428. <https://doi.org/10.1016/j.anucene.2020.107428>.
- Tiberga, M., Shafer, D., Lathouwers, D., Rohde, M., Kloosterman, J.L., 2019. Preliminary investigation on the melting behavior of a freeze-valve for the Molten Salt Fast Reactor. *Ann. Nucl. Energy* 132, 544–554. [https://doi.org/10.1016/j.anocene.2019.06.039](https://doi.org/10.1016/j.anucene.2019.06.039).
- Tominaga, Y., Stathopoulos, T., 2007. Turbulent Schmidt numbers for CFD analysis with various types of flowfield. *Atmos. Environ.* 41, 8091–8099. <https://doi.org/10.1016/j.atmosenv.2007.06.054>.
- Walker, S.A., Ji, W., 2021. Species transport analysis of noble metal fission product transport, deposition, and extraction in the molten salt reactor experiment. *Ann. Nucl. Energy* 158, 108250. [https://doi.org/10.1016/j.anocene.2021.108250](https://doi.org/10.1016/j.anucene.2021.108250).
- Wilcox, D.C., 2008. Formulation of the k-w Turbulence Model Revisited. *AIAA Journal* 46, 2823–2838. <https://doi.org/10.2514/1.36541>.